Coherent origin of peculiar radio pulsar polarization

Jarosław Dyks[1]

1. Nicolaus Copernicus Astronomical Center, Polish Academy of Sciences, Rabiańska 18, 87–100 Toruń, Poland

Radio pulsar data reveal a range of peculiar polarization phenomena, such as 1) jumps between orthogonal polarization modes (OPMs) that are coincident with both the maximum circular polarization fraction V/I and a non-vanishing linear polarization fraction L/I, 2) the same sign of V in both OPMs, 3) strong distortions of polarization angle (PA) from the rotating vector model (RVM) that are especially common in core components, and 4) non-orthogonal PA jumps. It is shown that these effects can be understood in terms of coherent addition of orthogonally polarized natural mode waves, with their relative phase lag and flux ratio being the key parameters that determine the apparent polarization. The phenomena can be efficiently studied with an empirical model which assumes that the emitted low-altitude signal is split into the natural propagation mode waves in a high-altitude 'intervening' region. The waves acquire a relative phase lag and combine coherently after they leave the region. In this model, the observed RVM-like PA curve is fixed by the B-field geometry at the high altitude, whereas the relative flux of the combining waves is parametrized by the mismatch of projected B-field geometry in the emission and intervening regions. Such approach has been successfully applied to peculiar polarization phenomena observed in PSR B1913+16, B1237+25, B1919+21 and B1933+16.

1 Introduction

Radio pulsar polarization exhibits many peculiar effects. In PSR B1913+16 (Weisberg & Taylor, 2002) and J1900−2600 (Johnston & Kerr, 2018) the polarization angle (PA) curve undergoes orthogonal displacement (jump) at pulse longitudes where the circular polarization fraction V/I is maximum and the linear polarization fraction L/I is larger than zero. This is opposite to the vanishing V and L expected from incoherent summation of two orthogonal elliptically polarized modes. High sensivity single pulse observations of other objects (Mitra et al., 2015) show that different samples observed in the same-mode PA track have either sign of V and that the same sign of V appears in both orthogonal PA tracks. Elliptical orthogonal modes are expected to bear opposite-sign V (and orthogonal PA). This suggests that the observed orthogonal polarization modes (OPMs) may not always be directly attributed to the elliptical natural propagation modes. Observed polarization phenomena also include other (nonorthogonal) distortions of the average PA curve from the standard S-swing of the rotating vector model (RVM), in which polarization is determined by the direction of the sky-projected magnetic field B. These distortions are often observed in the central (core) components of profiles (e.g. PSR B1237+25, B1933+16, B0329+54) and are associated with enhanced levels of V/I. Sudden jumps of PA by 45° are also observed within weakly polarized pulse intervals in B1919+21 (Mitra et al., 2015) and B0823+26 (Everett & Weisberg, 2001). All these striking effects

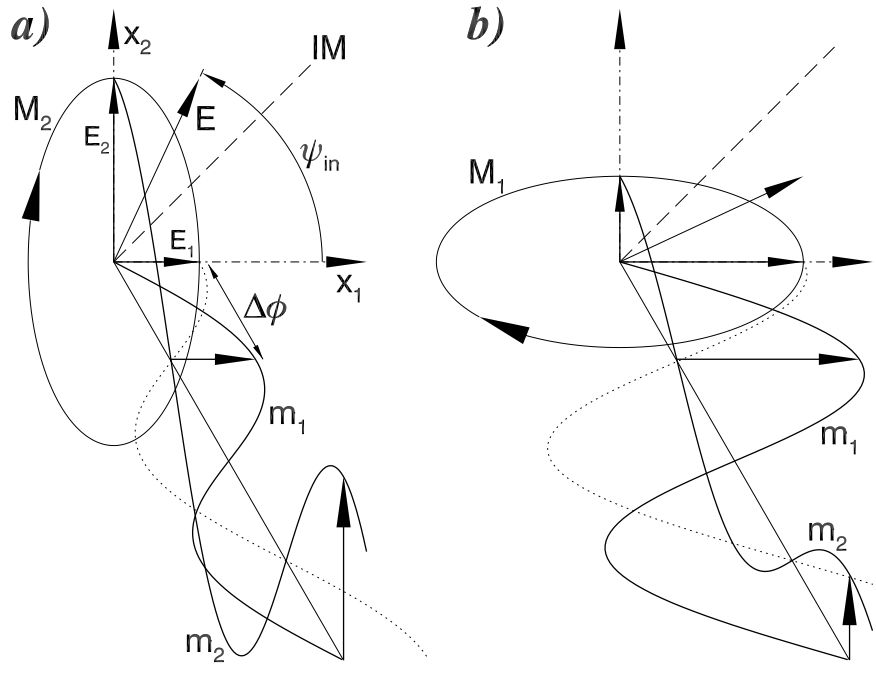

Fig. 1: The mechanism of producing two observed OPMs (M_1 and M_2) with the elliptical polarization of the same handedness (note the arrows at the ellipses that represent the modes). The OPMs result from coherent addition of the natural mode waves m_1 and m_2 that are induced by the incident signal $\vec{E}$ and phase delayed by $\Delta\phi$.

can be interpreted with an empirical model based on coherent addition of orthogonal linearly polarized natural mode waves (Dyks, 2017).

2 The nature of orthogonal polarization modes

The model assumes that a linearly polarized pulsar signal $\vec{E}$ in Fig. 1a, is emitted at a low radial distance $r_{\rm em}$ and penetrates some intervening region at higher altitude (radial distance $r_{\rm plr}$). The direction of $\vec{E}$ is misaligned at the angle $\psi_{\rm in}$ with respect to the principal polarization directions, $\vec{x}_1$ and $\vec{x}_2$, of the intervening region, so the signal is split into the orthogonal natural propagation mode waves (assumed to be linearly polarized). Because of small difference of their refraction index, the waves acquire a relative phase lag $\Delta\phi$. After leaving the region the waves combine into an elliptically polarized signal detected by a radio telescope.

Depending on the values of $\psi_{\rm in}$ and $\Delta\phi$ of the combining waves, a large diversity of PA, L/I and V/I may appear, as illustrated in Figs. 2 and 6 of Dyks (2017). However, when the phase lag $\Delta\phi$ is equal or close to $\pi/2$, the outgoing radiation is elliptically polarized along either one or another principal polarization direction ($\vec{x}_1$ or $\vec{x}_2$). The PA of the combined wave is determined by the orientation of the polarization ellipse major axis. Depending on whether the incident angle $\psi_{\rm in}$ is larger or smaller than 45°, the ensuing PA can either be equal to 0 (major axis along $\vec{x}_1$) or 90° (major axis aligned with $\vec{x}_2$). Thus, the question of which mode: M_1 or M_2 is

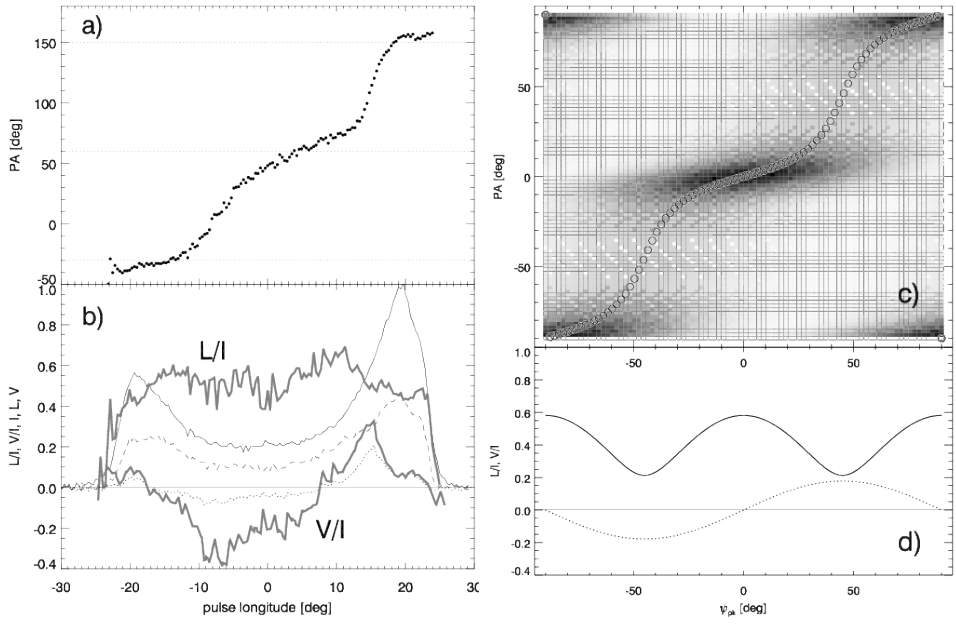

Fig. 2: Comparison of modelled polarization properties (right, Dyks 2017) to those observed in B1913+16 (left, after Weisberg & Taylor 2002). Modelled V/I is marked with the dotted line in panel **d**. Note that the maxima of $|V|$ coincide with the orthogonal PA transitions (top panels).

produced depends on which side of the dashed separatrix (IM in Fig. 1) the incident signal $\vec{E}$ is located. The emergence of particular mode thus depends on the ratio of magnitude of components E_1 and E_2, since $\tan\psi_{\rm in} = E_2/E_1$.

The coherent summation of natural mode waves thus creates two observed OPMs that are represented by the polarization ellipses M_1 and M_2 in Fig. 1. These OPMs have different polarization properties than the combining natural propagation modes (represented by the waves m_1 and m_2). In particular, the OPMs can have nonzero V of the same sign (handedness), which is the case for the parameters used in Fig. 1 (note the arrows at the ellipses M_1 and M_2).

The observed pulsar polarization depends on physical conditions in the emission region and the intervening region, with the latter possibly located at the polarization limiting altitude. These conditions (local plasma density and velocity, as well as the electric field) are highly unstable as evidenced by the erratic nature of pulsar radio emission. The main model parameters, i.e. $\psi_{\rm in}$ and $\Delta\phi$, are therefore drawn from statistical distributions $N_{\psi,{\rm in}}$ and $N_{\Delta\phi}$ which have the finite widths and are centered at $\psi_{\rm pk}$ and $\Delta\phi_{\rm pk}$, correspondingly. If $N_{\psi,{\rm in}}$ extends on both sides of the intermode separatrix ($\psi_{\rm in} = 45°$), then the strong OPMs appear whenever the lag distribution $N_{\Delta\phi}$ is reaching the quarter-cycle value of $\pi/2$.

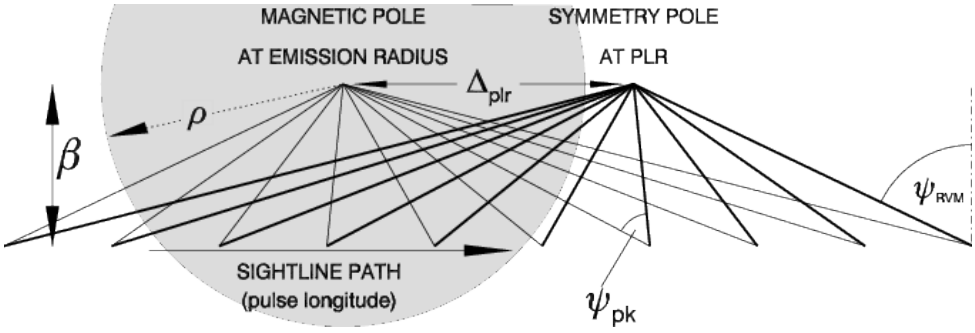

Fig. 3: Sky-projected polarization directions in the low-r emission region (thin lines radiating from the magnetic pole) and the high-r intervening region (PLR, thick lines). The patterns are separated by the angle $\Delta_{\rm plr}$. A sightline passing horizontally records the incident angle $\psi_{\rm in}$ between the two patterns (initially $\psi_{\rm in}$ is increasing, then decreasing). The RVM value of PA is determined by the absolute direction of the thick lines (measured with respect to a fixed reference direction, say the vertical). A circular pulsar beam of angular radius ρ (grey circle) is centered at the low-r magnetic pole on the left. The figure assumes dipolar B-field and the flat projection geometry (instead of spherical).

3 Polarization as a function of pulse longitude

To apply the model to pulsar data, it is necessary to formulate how $\psi_{\rm pk}$ and $\Delta\phi_{\rm pk}$ depend on the pulse longitude Φ. Interestingly, even simple ad hoc prescriptions produce polarization similar to that which is observed in some pulsars. The right hand side of Fig. 2 presents the PA curve (top), L/I (bottom, solid curve) and V/I (dotted line) calculated for fixed $\Delta\phi_{\rm pk} = 40^\circ$ and for $\psi_{\rm pk}$ that linearly increases with longitude, as marked on the horizontal axis. The 1-σ widths of Gaussian $N_{\psi,\rm in}$ and $N_{\Delta\phi}$ distributions were equal to 30° and 70°, respectively. These results qualitatively reproduce major polarization characteristics of B1913+16 (Fig. 2a). The PA curve has the step-like shape, L/I never reaches the close proximity of zero, and the OPM jumps occur at the maximum of V/I, which occurs when $\psi_{\rm pk}$ crosses the intermode separatrices at $\pm 45^\circ$.

The variations of PA in Fig. 2c appear because the misalignment between the polarization direction of the emitted signal ($\vec{E}$ in Fig. 1) and the intervening basis $(\vec{x}_1, \vec{x}_2)$ changes with the pulse longitude Φ. The result presented in Fig. 2 does not include any variations of PA that are caused by the rotation of the $(\vec{x}_1, \vec{x}_2)$ basis itself, i.e. the effect of the rotating vector model (RVM) is absent there. The RVM PA variations are determined by the geometry of plasma motion at the high altitude, where the intervening region (or the polarization-limiting region, PLR) is located. This geometry is governed by the corotation and the geometry of the high-altitude magnetic field, and it is known to produce the relativistic lag of the PA curve. This implies that the high altitude structure of polarization directions is displaced backward, toward later pulse longitudes. Therefore, the sky-projected polarization directions for the low $r_{\rm em}$ and the high $r_{\rm plr}$ may be presented as in the top part of Fig. 3. The projected B-field structure in the emission region (thin solid) is centered at the radio beam that is represented by the grey circle of angular radius ρ. The structure of PLR polarization directions (thick solid) is delayed by a small angle

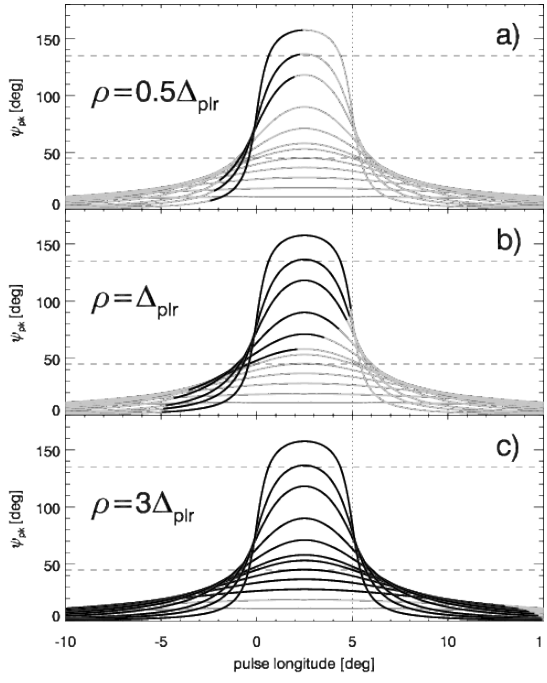

Fig. 4: Variations of incident angle $\psi_{\rm pk}$ with pulse longitude Φ, as calculated for $\beta/\Delta_{\rm plr}$ = 0.1, 0.2, 0.3, 0.5, 0.7, 0.9, 1.0, 1.2, 1.5, 2, 3, and 5. The central hump on the curves diminishes for larger β. Since the PLR symmetry point is delayed with respect to the radio beam center (see Fig. 3), only the black part of the curves is detectable. This detectable interval (pulse window) becomes wider for the increasing beam radius printed in the top left corner of each panel. The profile is centered at $\Phi = 0$, whereas the PLR symmetry point at $\Phi = \Delta_{\rm plr} = 5^\circ$.

$\Delta_{\rm plr}$. The incident angle $\psi_{\rm pk}$ (that corresponds to the peak of the $\psi_{\rm in}$ distribution) is measured between these two structures at the location selected by the traversing line of sight. The RVM value of PA, i.e. $\psi_{\rm RVM}$, is measured between the thick solid lines and the vertical (main meridional) direction. The observed PA is equal to $\psi_{\rm obs} = \psi + \psi_{\rm RVM}$, where $\psi = \psi(\psi_{\rm pk}, \Delta\phi)$ results from the coherent summation of the natural mode waves. The model result of Fig. 2 presents ψ, i.e. it only includes the variations of $\psi_{\rm pk}$, while the rotation of the thick lines in Fig. 3 (RVM) is ignored.

As shown in Fig. 3, $\psi_{\rm pk}$ is increasing with pulse longitude, until the sightline is half way between the emission pole and the PLR symmetry pole. Then $\psi_{\rm pk}$ starts to decrease in symmetrical way. The full range of $\psi_{\rm pk}$ depends on the ratio between the impact angle (β in Fig. 3) and the PLR displacement $\Delta_{\rm plr}$. Different curves in Fig. 4 correspond to $\beta/\Delta_{\rm plr}$ in the range between 0.1 and 5. The lowest (most flat) cases correspond to large β (distant passage of sightline) or to the small PLR displacement ($\beta \ll \Delta_{\rm plr}$). When the sightline is passing close to the pole (or $\Delta_{\rm plr}$ is large), $\psi_{\rm pk}$ reaches large values in the pulse interval between the profile center (located at $\Phi = 0$ in Fig. 4) and the steepest gradient of the RVM PA (i.e. the PLR symmetry center, at $\Phi = 5^\circ$, dotted vertical). In this last case $\psi_{\rm pk}$ may be crossing the intermodal separatrix (at $\psi_{\rm in} = 45^\circ$ or 135°) a few times within the pulse window, which leads to the OPM jumps, such as those described above for B1913+16. When $\Delta_{\rm plr}$ is small, the horizontal scale of Fig. 3 is narrow (see Fig. 18 in Dyks 2017), hence the fast and multiple intermode crossings occur near the profile center. As discussed by Dyks (2017) these excursions of $\psi_{\rm pk}$ must be responsible for the circularly polarized 'loop-shaped' distortions of a PA curve, which are often observed at the cores of profiles

(e.g. PSR B1237+25, B1933+16). In these phenomena, the maxima of V/I coincide with minimal L/I value, which is consistent with the coherent mode addition model. Because the $\psi_{\rm pk}(\Phi)$ profiles are mirror-symmetric, the variations of core polarization may occur in a forth-and-back way, with some polarization characteristics retreating at a later pulse longitude (which is the case for the 'failed' OPM transition in the PA loop of B1933+16) or they can be repeated (e.g. the twin minima of L/I in the last mentioned pulsar). However, asymmetric phenomena, such as antisymmetric V/I profile that is often observed at the core (e.g. in B1237+25) can also appear in the empirical model of the coherent mode addition.

Regardless of the actual radio beam pattern, in most pulsars the bright (detectable) radio emission is likely to concentrate near the magnetic pole. Accordingly, a circular beam of angular radius ρ is centered at the magnetic pole in Fig. 3 (grey circle). This implies that only an asymmetric fragment of the full $\psi_{\rm pk}$ profile is detectable within the pulse window. As shown in different panels of Fig. 4, that detectable part (marked black) becomes wider for the increasing ratio of $\rho/\Delta_{\rm plr}$. This effect provides large diversity of possible cases, with $\psi_{\rm pk}$ either increasing monotonically (Fig. 4 a and b) or changing nonmonotonically within the pulse window (Fig. 4 b and c). The monotonic changes of $\psi_{\rm pk}$ have appeared suitable to interpret the polarization of B1913+16, whereas the nonmonotonic changes can model the core polarization of B1933+16 and B1237+25 (including the antisymmetric V/I profile in the core of the latter object). More informations on the coherent mode addition, and description of the 45° PA jump are provided by Dyks (2017) .

Acknowledgements. The research was supported by the National Science Centre, Poland (DEC-2011/02/A/ST9/00256). I thank NCAC PAS for funding my participation in 38$^{\rm th}$ PAS assembly.

References

Dyks, J., *MNRAS* **472**, 4598 (2017)

Everett, J. E., Weisberg, J. M., *ApJ* **553**, 341 (2001)

Johnston, S., Kerr, M., *MNRAS* **474**, 4629 (2018)

Mitra, D., Arjunwadkar, M., Rankin, J. M., *ApJ* **806**, 236 (2015)

Weisberg, J. M., Taylor, J. H., *ApJ* **576**, 942 (2002)